

Exposure Bracketing is All You Need for Unifying Image Restoration and Enhancement Tasks

Zhilu Zhang¹, Shuohao Zhang¹, Renlong Wu¹, Zifei Yan¹, Wangmeng Zuo¹

¹Harbin Institute of Technology, Harbin, China

cszlzhang@outlook.com, yhyzshrby@163.com, hirenlongwu@gmail.com,
{yanzifei, wmzuo}@hit.edu.cn

Abstract. It is highly desired but challenging to acquire high-quality photos with clear content in low-light environments. Although multi-image processing methods (using burst, dual-exposure, or multi-exposure images) have made significant progress in addressing this issue, they typically focus on specific restoration or enhancement problems, being insufficient in exploiting multi-image. Motivated by that multi-exposure images are complementary in denoising, deblurring, high dynamic range imaging, and super-resolution, we propose to utilize exposure bracketing photography to unify restoration and enhancement tasks in this work. Due to the difficulty in collecting real-world pairs, we suggest a solution that first pre-trains the model with synthetic paired data and then adapts it to real-world unlabeled images. In particular, a temporally modulated recurrent network (TMRNet) and self-supervised adaptation method are proposed. Moreover, we construct a data simulation pipeline to synthesize pairs and collect real-world images from 200 night-time scenarios. Experiments on both datasets show that our method performs favorably against the state-of-the-art multi-image processing ones. The dataset, code, and pre-trained models are available at <https://github.com/cszhilu1998/BracketIRE>.

Keywords: Exposure bracketing · Image restoration and enhancement

1 Introduction

In low-light environments, capturing visually appealing photos with clear content presents a highly desirable yet challenging goal. When adopting a low exposure time, the camera only captures a small amount of photons, introducing inevitable noise and rendering dark areas invisible. When taking a high exposure time, camera shake and object movement result in blurry images, in which bright areas may be overexposed. Although single-image restoration (*e.g.*, denoising [1, 7, 27, 44, 95, 98, 99], deblurring [13, 54, 59, 74, 96, 97], and super-resolution (SR) [18, 41, 45–47, 100, 102]) and enhancement (*e.g.*, high dynamic range (HDR) reconstruction [11, 22, 42, 49, 64, 107]) methods have been extensively investigated, their performance is constrained by the severely ill-posed problems.

Table 1: Comparison between various multi-image processing manners.

Setting	Methods	Input Images	Supported Tasks				
			Denoising	Deblurring	HDR	SR	
Burst Denoising	[26, 28, 56, 68, 89]	Burst	✓				
Burst Deblurring	[2, 15, 63, 84]			✓			
Burst SR	[16, 83, 85]					✓	
Burst Denoising and SR	[3–6, 19, 20, 40, 53, 55, 86]			✓		✓	
Burst Denoising and HDR	[23, 30]			✓		✓	
Dual-Exposure Image Restoration	[10, 37, 57, 69, 94, 105, 106]	Dual-Exposure	✓	✓			
Basic HDR Imaging	[33, 50, 61, 75, 91, 92, 103]	Multi-Exposure				✓	
HDR Imaging with Denoising	[12, 48, 64]		✓			✓	
HDR Imaging with SR	[73]					✓	✓
HDR Imaging with Denoising and SR	[39]		✓			✓	✓
Our BracketIRE	-	Multi-Exposure	✓	✓	✓	✓	
Our BracketIRE+			✓	✓	✓	✓	

Recently, leveraging multiple images for image restoration and enhancement has demonstrated potential in addressing this issue, thereby attracting increasing attention. We provide a summary of several related settings and methods in Tab. 1. For example, some burst image restoration methods [3–6, 19, 20, 40, 53, 55, 86] utilize multiple consecutive frames with the same exposure time as inputs, being able to perform SR and denoising. The works based on dual-exposure images [10, 37, 57, 69, 94, 105, 106] combine the short-exposure noisy and long-exposure blurry pairs for better restoration. Multi-exposure images are commonly employed for HDR imaging [33, 50, 61, 65, 72, 75, 87, 91, 92, 103].

Nevertheless, in night scenarios, it remains unfeasible to obtain noise-free, blur-free, and HDR images when employing these multi-image processing methods. On the one hand, burst and dual-exposure images both possess restricted dynamic ranges, constraining the potential expansion of the two manners into HDR reconstruction. On the other hand, most HDR reconstruction approaches based on multi-exposure images are constructed with the ideal assumption that image noise and blur are not taken into account, which results in their inability to restore degraded images. Although recent works [12, 39, 48] have combined with denoising task, blur in long-exposure images has not been incorporated into them, which is still inconsistent with real-world multi-exposure images.

In fact, considering all multi-exposure factors (including noise, blur, underexposure, overexposure, and misalignment) is not only beneficial to practical applications, but also offers us an opportunity to unify image restoration and enhancement tasks. **First**, the independence and randomness of noise [82] between images allow them to assist each other in denoising, and its motivation is similar to that of burst denoising [26, 28, 56, 68, 89]. In particular, as demonstrated in dual-exposure restoration works [10, 37, 57, 69, 94, 105, 106], long-exposure images with a higher signal-to-noise ratio can play a significantly positive role in removing noise from the short-exposure images. **Second**, the shortest-exposure image can be considered blur-free. It can offer sharp guidance for deblurring longer-exposure images. **Third**, underexposed areas in the short-exposure image may be well-exposed in the long-exposure one, while overexposed regions

in the long-exposure image may be clear in the short-exposure one. Combining multi-exposure images makes HDR imaging easier than single-image enhancement. **Fourth**, the sub-pixel shift between multiple images caused by camera shake or motion is conducive to multi-frame SR [85]. In summary, leveraging the complementarity of multi-exposure images offers the potential to integrate the four problems (*i.e.*, denoising, deblurring, HDR reconstruction, and SR) into a unified framework that can generate a noise-free, blur-free, high dynamic range, and high-resolution image.

Specifically, in terms of tasks, we first utilize bracketing photography to unify basic restoration (*i.e.*, denoising and deblurring) and enhancement (*i.e.*, HDR reconstruction), named BracketIRE. Then we append the SR task, dubbed BracketIRE+, as shown in Tab. 1. In terms of methods, due to the difficulty of collecting real-world paired data, we achieve that through supervised pre-training on synthetic pairs and self-supervised adaptation on real-world images. On the one hand, we adopt the recurrent network manner as the basic framework, which is inspired by its successful applications in processing sequence images, *e.g.*, burst [28, 68, 86] and video [8, 9, 77] restoration. Nevertheless, sharing the same restoration parameters for each frame may result in limited performance, as degradations (*e.g.*, blur, noise, and color) vary between different multi-exposure images. To alleviate this problem, we propose a temporally modulated recurrent network (TMRNet), where each frame not only shares some parameters with others, but also has its own specific ones. On the other hand, pre-trained TMRNet on synthetic data has limited generalization ability and sometimes produces unpleasant artifacts in the real world, due to the inevitable gap between simulated and real images. For that, we propose a self-supervised adaptation method. In particular, we utilize the temporal characteristics of multi-exposure image processing to design learning objectives to fine-tune TMRNet.

For training and evaluation, we construct a pipeline for synthesizing data pairs, and collect real-world images from 200 nighttime scenarios with a smartphone. The two datasets also provide benchmarks for future studies. We conduct extensive experiments, which show that the proposed method achieves state-of-the-art performance in comparison with other multi-image processing ones.

The contributions can be summarized as follows:

- We propose to utilize exposure bracketing photography to unify image restoration and enhancement tasks, including image denoising, deblurring, high dynamic range reconstruction, and super-resolution.
- We suggest a solution that first pre-trains the model with synthetic pairs and then adapts it to unlabeled real-world images, where a temporally modulated recurrent network and a self-supervised adaptation method are proposed.
- We construct a data simulation pipeline and collect real-world nighttime images. Experiments on both datasets show the proposed method outperforms the state-of-the-art multi-image processing ones.

2 Related Work

2.1 Supervised Multi-Image Processing.

Burst Image Restoration and Enhancement. Burst-based manners generally leverage multiple consecutive frames with the same exposure for image processing. Most methods focus on image restoration, such as denoising, deblurring, and SR tasks, as shown in Tab. 1. And they mainly explore inter-frame alignment and feature fusion manners. The former can be implemented by utilizing various techniques, *e.g.*, homography transformation [83], optical flow [4, 5, 67], deformable convolution [14, 20, 28, 53], and cross-attention [55]. The latter are also developed with multiple routes, *e.g.*, weighted-based mechanism [4, 5], kernel prediction [56, 89], attention-based merging [20, 55], and recursive fusion [16, 28, 68, 86]. Moreover, HDR+ [30] joins HDR imaging and denoising by capturing underexposure raw bursts. Recent updates [23] of HDR+ introduce additional well-exposed frames for improving performance. Although such manners may be suitable for scenes with moderate dynamic range, they have limited ability for scenes with high dynamic range.

Dual-Exposure Image Restoration. Several methods [10, 37, 57, 69, 94, 105, 106] exploit the complementarity of short-exposure noisy and long-exposure blurry images for better restoration. For example, Yuan *et al.* [94] estimates blur kernels by exploring the texture of short-exposure images and then employ the kernels to deblur long-exposure ones. Mustaniemi *et al.* [57] and Chang *et al.* [10] deploy convolutional neural networks (CNN) to aggregate dual-exposure images, achieving superior results compared with single-image methods on synthetic data. D2HNet [106] proposes a two-phase DeblurNet-EnhanceNet architecture for real-world image restoration. However, few works join it with HDR imaging, mainly due to the restricted dynamic range of dual-exposure images.

Multi-Exposure HDR Image Reconstruction. Multi-exposure images are widely used for HDR image reconstruction. Most methods [33, 50, 61, 65, 72, 75, 87, 91, 92, 103] only focus on removing ghosting caused by image misalignment. For instance, Kalantari [33] align multi-exposure images and then propose a data-driven approach to merge them. AHDRNet [92] utilizes spatial attention and dilated convolution to achieve deghosting. HDR-Transformer [50] and SCTNet [75] introduce self-attention and cross-attention to enhance feature interaction, respectively. Besides, a few methods [12, 48, 64] take noise into account. Kim *et al.* [35] further introduce motion blur in the long-exposure image. However, the unrealistic blur simulation approach and the requirements of time-varying exposure sensors limit its practical applications. In this work, we consider more realistic situations in low-light environments, and incorporate both severe noise and blur. More importantly, we propose to utilize the complementary potential of multi-exposure images to unify image restoration and enhancement tasks, including image denoising, deblurring, HDR reconstruction, and SR.

2.2 Self-Supervised Multi-Image Processing

The complementarity of multiple images enables the achievement of certain image processing tasks in a self-supervised manner. For self-supervised image restoration, some works [17, 21, 70, 81] accomplish multi-frame denoising with the assistance of Noise2Noise [43] or blind-spot networks [36, 38, 88]. SelfIR [105] employs a collaborative learning framework for restoring noisy and blurry images. Bhat *et al.* [6] propose self-supervised Burst SR by establishing a reconstruction objective that models the relationship between the noisy burst and the clean image. Self-supervised real-world SR can also be addressed by combining short-focus and telephoto images [78, 90, 104]. For self-supervised HDR reconstruction, several works [60, 66, 93] generate or search pseudo-pairs for training the model, while SelfHDR [103] decomposes the potential GT into constructable color and structure supervision.

However, these methods can only handle specific degradations, making them less practical for our task with multiple ones. In this work, instead of creating self-supervised algorithms trained from scratch, we suggest adapting the model trained on synthetic pairs to real images, and utilize the temporal characteristics of multi-exposure image processing to design self-supervised learning objectives.

3 Method

3.1 Problem Definition and Formulation

Denote the scene irradiance at time t by $\mathbf{X}(t)$. When capturing a raw image \mathbf{Y} at t_0 time, we can simplify the camera’s image formation model as,

$$\mathbf{Y} = S\left(\int_{t_0}^{t_0+\Delta t} D(W_t(\mathbf{X}(t)))dt + \mathbf{N}\right). \quad (1)$$

In this equation, (1) D is a spatial sampling function, which is mainly related to sensor size. This function limits the image resolution. (2) Δt denotes exposure time and W_t represents the warp operation that accounts for camera shake. Combined with potential object movements in $\mathbf{X}(t)$, the integral formula \int can result in a blurry image, especially when Δt is long [59]. (3) \mathbf{N} represents the inevitable noise, *e.g.*, read and shot noise [7]. (4) S maps the signal to integer values ranging from 0 to $2^b - 1$, where b denotes the bit depth of the sensor. This mapping may reduce the dynamic range of the scene [39]. In summary, the imaging process introduces multiple degradations, including blur, noise, as well as a decrease in dynamic range and resolution. Notably, in low-light conditions, some degradations (*e.g.*, noise) may be more severe.

In pursuit of higher-quality images, substantial efforts have been made in dealing with the inverse problem through single-image or multi-image restoration (*i.e.*, denoising, deblurring, and SR) and enhancement (*i.e.*, HDR imaging). However, most efforts tend to focus on addressing partial degradations, and few works encompass all these aspects, as shown in Tab. 1. In this work, inspired

by the complementary potential of multi-exposure images, we propose to exploit bracketing photography to integrate and unify these tasks for obtaining noise-free, blur-free, high dynamic range, and high-resolution images.

Specifically, the proposed BracketIRE involves denoising, deblurring, and HDR reconstruction, while BracketIRE+ adds support for SR task. Here, we provide a formalization for them. Firstly, We define the number of input multi-exposure images as T , and define the raw image taken with exposure time Δt_i as \mathbf{Y}_i , where $i \in \{1, 2, \dots, T\}$ and $\Delta t_i < \Delta t_{i+1}$. Then, we follows the recommendations from multi-exposure HDR reconstruction methods [50, 61, 75, 91, 92], normalizing \mathbf{Y}_i to $\frac{\mathbf{Y}_i}{\Delta t_i/\Delta t_1}$ and concatenating it with its gamma-transformed image, *i.e.*,

$$\mathbf{Y}_i^c = \left\{ \frac{\mathbf{Y}_i}{\Delta t_i/\Delta t_1}, \left(\frac{\mathbf{Y}_i}{\Delta t_i/\Delta t_1} \right)^\gamma \right\}, \quad (2)$$

where γ represents the gamma correction parameter and is generally set to 1/2.2. Finally, we feed these concatenated images into BracketIRE or BracketIRE+ model \mathcal{B} with parameters $\Theta_{\mathcal{B}}$, *i.e.*,

$$\hat{\mathbf{X}} = \mathcal{B}(\{\mathbf{Y}_i^c\}_{i=1}^T; \Theta_{\mathcal{B}}), \quad (3)$$

where $\hat{\mathbf{X}}$ is the generated image. Furthermore, the optimized network parameters can be written as,

$$\Theta_{\mathcal{B}}^* = \arg \min_{\Theta_{\mathcal{B}}} \mathcal{L}_{\mathcal{B}}(\mathcal{T}(\hat{\mathbf{X}}), \mathcal{T}(\mathbf{X})), \quad (4)$$

where $\mathcal{L}_{\mathcal{B}}$ represents the loss function, and can adopt ℓ_1 loss. \mathbf{X} is the ground-truth (GT) image. $\mathcal{T}(\cdot)$ denotes the tone-mapping operator, *i.e.*,

$$\mathcal{T}(\mathbf{X}) = \frac{\log(1 + \mu\mathbf{X})}{\log(1 + \mu)}, \text{ where } \mu = 5,000. \quad (5)$$

Besides, we consider the shortest-exposure image (*i.e.*, \mathbf{Y}_1) blur-free and take it as a spatial alignment reference for other frames. In other words, the output $\hat{\mathbf{X}}$ should be aligned strictly with \mathbf{Y}_1 .

Towards real-world dynamic scenarios, it is nearly impossible to capture GT \mathbf{X} , while it is hard to develop self-supervised algorithms trained on real-world images from scratch. To address the issue, we suggest pre-training the model on synthetic pairs first and then adapting it to real-world scenarios in a self-supervised manner. In particular, we propose a temporally modulated recurrent network for BracketIRE and BracketIRE+ tasks in Sec. 3.2, and a self-supervised adaptation method in Sec. 3.3.

3.2 Temporally Modulated Recurrent Network

Recurrent networks have been successfully applied to burst [86] and video [8, 9, 77] restoration methods, which generally involve four modules, *i.e.*, feature extraction, alignment, aggregation, and reconstruction module. Here we adopt a uni-directional recurrent network as our baseline, and briefly describe its pipeline.

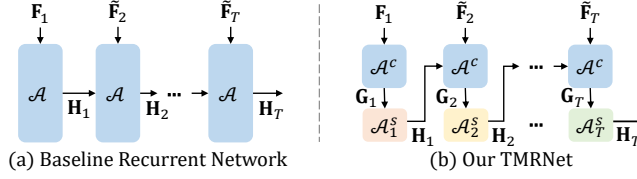


Fig. 1: Illustration of baseline recurrent network and our TMRNet. Instead of sharing parameters of aggregation module \mathcal{A} for all frames, we divide it into a common one \mathcal{A}^c for all frames and a specific one \mathcal{A}_i^s only for i -th frame.

Firstly, the multi-exposure images $\{\mathbf{Y}_i^c\}_{i=1}^T$ are fed into an encoder for extracting features $\{\mathbf{F}_i\}_{i=1}^T$. Then, the alignment module is deployed to align \mathbf{F}_i with reference feature \mathbf{F}_1 , getting the aligned feature $\tilde{\mathbf{F}}_i$. Next, the aggregation module \mathcal{A} takes $\tilde{\mathbf{F}}_i$ and the previous temporal feature \mathbf{H}_{i-1} as inputs, generating the current fused feature \mathbf{H}_i , *i.e.*,

$$\mathbf{H}_i = \mathcal{A}(\tilde{\mathbf{F}}_i, \mathbf{H}_{i-1}; \Theta_{\mathcal{A}}), \quad (6)$$

where $\Theta_{\mathcal{A}}$ denotes the parameters of \mathcal{A} . Finally, \mathbf{H}_T is fed into the reconstruction module to output the result.

The aggregation module plays a crucial role in the recurrent framework and usually takes up most of the parameters. In burst and video restoration tasks, the degradation types of multiple input frames are generally the same, so it is appropriate for frames to share the same aggregation network parameters $\Theta_{\mathcal{A}}$. In BracketIRE and BracketIRE+ tasks, the noise models of multi-exposure images may be similar, as they can be taken by the same device. However, other degradations are varying. For example, the longer the exposure time, the more serious the image blur, the fewer underexposed areas, and the more overexposed ones. Thus, sharing $\Theta_{\mathcal{A}}$ may limit performance.

To alleviate this problem, we suggest assigning specific parameters for each frame while sharing some ones, thus proposing a temporally modulated recurrent network (TMRNet). As shown in Fig. 1, we divide the aggregation module \mathcal{A} into a common one \mathcal{A}^c for all frames and a specific one \mathcal{A}_i^s only for i -th frame. Features are first processed via \mathcal{A}^c and then further modulated via \mathcal{A}_i^s . Eq. (6) can be modified as,

$$\begin{aligned} \mathbf{G}_i &= \mathcal{A}^c(\tilde{\mathbf{F}}_i, \mathbf{H}_{i-1}; \Theta_{\mathcal{A}^c}), \\ \mathbf{H}_i &= \mathcal{A}_i^s(\mathbf{G}_i; \Theta_{\mathcal{A}_i^s}), \end{aligned} \quad (7)$$

where \mathbf{G}_i represents intermediate features, $\Theta_{\mathcal{A}^c}$ and $\Theta_{\mathcal{A}_i^s}$ denote the parameters of \mathcal{A}^c and \mathcal{A}_i^s , respectively. We do not design complex architectures for \mathcal{A}^c and \mathcal{A}_i^s , and each one only consists of a 3×3 convolution layer followed by some residual blocks [31]. More details of TMRNet can be seen in Sec. 5.1.

3.3 Self-Supervised Real-Image Adaptation

It is hard to simulate multi-exposure images with diverse variables (*e.g.*, noise, blur, brightness, and movement) that are completely consistent with real-world

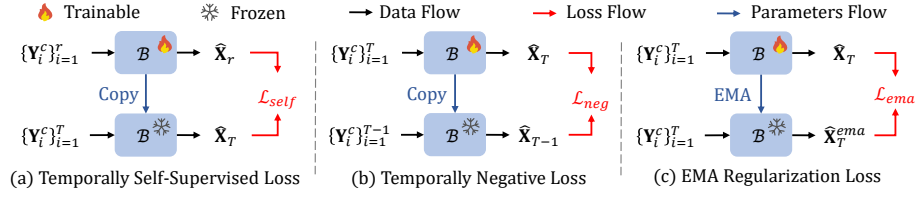


Fig. 2: Self-supervised loss terms for real-image adaptation. \mathcal{B} denotes TMRNet for BracketIRE or BracketIRE+ task. In sub-figure (a), an integer from 1 to $T - 1$ is randomly chosen as r . In sub-figure (c), EMA denotes exponential moving average.

ones. Due to the inevitable gap, models trained on synthetic pairs have limited generalization capabilities in real scenarios. Undesirable artifacts are sometimes produced. To address the issue, we propose to perform self-supervised adaptation for real-world unlabeled images.

Specifically, we explore the temporal characteristics of multi-exposure image processing to design self-supervised loss terms elaborately, as shown in Fig. 2. Denote the model output of inputting the previous r frames $\{\mathbf{Y}_i^c\}_{i=1}^r$ by $\hat{\mathbf{X}}_r$. Generally, $\hat{\mathbf{X}}_T$ performs better than $\hat{\mathbf{X}}_r$ ($r \in [1, T - 1]$). For supervising $\hat{\mathbf{X}}_r$, although no ground-truth is provided, $\hat{\mathbf{X}}_T$ can be taken as the pseudo-target. Thus, the temporally self-supervised loss can be written as,

$$\mathcal{L}_{self} = \|\mathcal{T}(\hat{\mathbf{X}}_r) - \mathcal{T}(sg(\hat{\mathbf{X}}_T))\|_1, \quad (8)$$

where r is randomly selected from 1 to $T - 1$, $sg(\cdot)$ denotes the stop-gradient operator. In addition, as the number of input frames increases, the improvement of adding frames may become slight (similar to the law of diminishing marginal effects). To prevent $\hat{\mathbf{X}}_T$ and $\hat{\mathbf{X}}_{T-1}$ from being too close and indistinguishable, we set the constraint \mathcal{L}_{neg} to push them away. Thus, $\hat{\mathbf{X}}_{T-1}$ can be as negative sample of $\hat{\mathbf{X}}_T$, and the temporally negative loss can be written as,

$$\mathcal{L}_{neg} = -\|\mathcal{T}(\hat{\mathbf{X}}_T) - \mathcal{T}(sg(\hat{\mathbf{X}}_{T-1}))\|_1. \quad (9)$$

Nevertheless, only deploying \mathcal{L}_{self} and \mathcal{L}_{neg} can easily lead to trivial solutions. To stabilize training process, we suggest an exponential moving average (EMA) regularization loss, which constrains the output of current iteration to be not too far away from that of previous ones. It can be written as,

$$\mathcal{L}_{ema} = \|\mathcal{T}(\hat{\mathbf{X}}_T) - \mathcal{T}(sg(\hat{\mathbf{X}}_T^{ema}))\|_1, \quad (10)$$

where $\hat{\mathbf{X}}_T^{ema} = \mathcal{B}(\{\mathbf{Y}_i^c\}_{i=1}^T; \Theta_{\mathcal{B}}^{ema})$ and $\Theta_{\mathcal{B}}^{ema}$ denotes EMA parameters in the current iteration. Denote model parameters in the k -th iteration by $\Theta_{\mathcal{B}_k}$, the EMA parameters in the k -th iteration can be written as,

$$\Theta_{\mathcal{B}_k}^{ema} = a\Theta_{\mathcal{B}_{k-1}}^{ema} + (1 - a)\Theta_{\mathcal{B}_k}, \quad (11)$$

where $\Theta_{\mathcal{B}_0}^{ema} = \Theta_{\mathcal{B}_0}$ and $a = 0.999$.

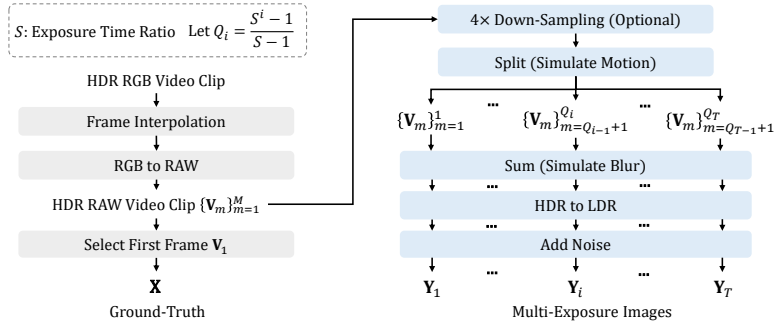


Fig. 3: Overview of data simulation pipeline. We utilize HDR video to synthesize multi-exposure images $\{\mathbf{Y}_i\}_{i=1}^T$ and the corresponding GT image \mathbf{X} . S denotes the exposure time ratio between \mathbf{Y}_i and \mathbf{Y}_{i-1} . \mathbf{Y}_i is obtained by summing and processing S^{i-1} ($i-1$)-th power of S) images from HDR raw video \mathbf{V} . Q_i denotes the total number of images from \mathbf{V} that participate in constructing $\{\mathbf{Y}_k\}_{k=1}^i$.

The total adaptation loss is the combination of \mathcal{L}_{ema} , \mathcal{L}_{self} , and \mathcal{L}_{neg} , *i.e.*,

$$\mathcal{L}_{ada} = \mathcal{L}_{ema} + \lambda_{self}\mathcal{L}_{self} + \lambda_{neg}\mathcal{L}_{neg}, \quad (12)$$

where λ_{self} and λ_{neg} are set to 1 and 0.2, respectively.

4 Datasets

4.1 Synthetic Paired Dataset

Although it is unrealistic to synthesize perfect multi-exposure images, we should still shorten the gap with the real images as much as possible. In the camera’s imaging model in Eq. (1), noise, blur, motion, and dynamic range of multi-exposure images should be carefully designed.

Video provides a better basis than single-image in simulating motion and blur of multi-exposure images. We start with HDR videos from Froehlich *et al.* [24] to construct the simulation pipeline, as shown in Fig. 3. First, we follow the suggestion from Nah *et al.* [58] to perform frame interpolation, as these low frame rate (~ 25 fps) videos are not suitable for synthesizing blur directly. RIFE [32] is adopted for increasing the frame rate by 32 times. Then, we convert these RGB videos to raw space with Bayer pattern according to UPI [7], getting HDR raw sequences $\{\mathbf{V}_m\}_{m=1}^M$. The first frame \mathbf{V}_1 is taken as a GT image.

Next, we utilize $\{\mathbf{V}_m\}_{m=1}^M$ and introduce degradations to construct multi-exposure images. The process mainly includes the following 5 steps. (1) Bicubic $4\times$ down-sampling is applied to obtain low-resolution images, which is optional and serves for BracketIRE+ task. (2) The video is split into T non-overlapped groups, where i -th group should be used to synthesize \mathbf{Y}_i . Such grouping utilizes the motion in the video itself to simulate motion between T multi-exposure images. (3) Denote the exposure time ratio between \mathbf{Y}_i and \mathbf{Y}_{i-1} by S . We

sequentially move S^{i-1} ($\{i-1\}$ -th power of S) consecutive images into the above i -th group, and sum them up to simulate blurry images. (4) We transform the HDR blurry images into low dynamic range (LDR) ones by cropping values outside the specified range and mapping the cropped values to 10-bit unsigned integers. (5) We add the heteroscedastic Gaussian noise [7, 29, 79] to LDR images to generate the final multi-exposure images (*i.e.*, $\{\mathbf{Y}_i\}_{i=1}^T$). The noise variance is a function of pixel intensity, whose parameters are estimated from the captured real-world images in Sec. 4.2. More noise details can be seen in the suppl.

Besides, we set the exposure time ratio S to 4 and the frame number T to 5, as it can cover most of the dynamic range with fewer images. The resolution of GT is $1,920 \times 1,080$. Finally, we obtain 1,335 data pairs from 35 scenes. 1,045 pairs from 31 scenes are used for training, and the remaining 290 pairs from the other 4 scenes are used for testing.

4.2 Real-World Dataset

Real-world multi-exposure images are collected with the main camera of Xiaomi 10S smartphone at night. Specifically, we utilize the bracketing photography function in ProShot [25] application (APP) to capture raw images with a resolution of $6,016 \times 4,512$. The exposure time ratio S is set to 4, the frame number T is set to 5, ISO is set to 1,600; these values are also the maximum available settings in APP. The exposure time of the medium-exposure image (*i.e.*, \mathbf{Y}_3) is automatically adjusted by APP. Thus, other exposures can be obtained based on S . It is worth noting that we hold the smartphone for shooting, without any stabilizing device, which aims to bring in the realistic hand-held shake. Besides, both static and dynamic scenes are collected, with a total of 200. 100 scenes are used for training and the other 100 are used for evaluation.

5 Experiments

5.1 Implementation Details

Network Details. The input and output are both raw images with the Bayer pattern. Following settings in RBSR [86], the encoder and reconstruction module consist of 5 residual blocks [31], the alignment module adopts flow-guided deformable approach [9]. Besides, the total number of residual blocks in aggregation module remains the same as that of RBSR [86], *i.e.*, 40, where the common module has 16 and the specific one has 24. For BracketIRE+ task, we additionally deploy PixelShuffle [71] at the end of networks for up-sampling features.

Training Details. We randomly crop patches and augment them with flips and rotations. The batch size is set to 8. The input patch size is 128×128 and 64×64 for BracketIRE and BracketIRE+ tasks, respectively. We adopt AdamW [52] optimizer with $\beta_1 = 0.9$ and $\beta_2 = 0.999$. Models are trained for 400 epochs on synthetic images and fine-tuned for 10 epochs on real-world ones, with the initial learning rate of 10^{-4} and 7.5×10^{-5} , respectively. Cosine annealing strategy [51] is employed to decrease the learning rates to 10^{-6} . All experiments are conducted with PyTorch [62] on a single Nvidia RTX A6000 GPU.

Table 2: Quantitative comparison with state-of-the-art methods on the synthetic and real-world datasets of BracketIRE and BracketIRE+ tasks, respectively. The top two results are marked in **bold** and underlined, respectively.

Method	BracketIRE		BracketIRE+		
	Synthetic	Real-World	Synthetic	Real-World	
	PSNR \uparrow /SSIM \uparrow /LPIPS \downarrow	CLIP-IQA \uparrow /MUSIQ \uparrow	PSNR \uparrow /SSIM \uparrow /LPIPS \downarrow	CLIP-IQA \uparrow /MUSIQ \uparrow	
Burst Processing Networks	DBSR [4]	34.03/0.9012/0.188	0.1678/25.271	28.21/0.8364/0.338	0.3460/20.182
	MFIR [5]	34.67/0.9121/0.175	0.2219/24.549	28.40/0.8424/0.320	0.3538/20.060
	BIPNet [19]	35.98/0.9314/0.145	0.2252/25.253	28.41/0.8432/0.326	0.3605/19.073
	Burstormer [20]	36.62/0.9378/0.140	0.2424/25.754	28.37/0.8460/0.301	0.3642/19.473
	RBSR [86]	37.88/ <u>0.9453</u> /0.119	0.2231/26.837	<u>28.70/0.8549</u> /0.279	0.3551/21.540
HDR Reconstruction Networks	AHDRNet [92]	36.32/0.9273/0.154	0.2006/25.082	28.17/0.8422/0.309	0.3466/19.476
	HDRGAN [61]	35.05/0.9161/0.175	0.2049/23.943	28.35/0.8423/0.338	<u>0.3648</u> /19.159
	HDR-Tran. [50]	36.54/0.9341/0.127	0.2062/25.610	28.15/0.8482/0.281	0.3317/20.201
	SCTNet [75]	36.90/0.9437/0.120	0.2365/26.350	28.28/0.8461/0.282	0.3514/20.115
	Kim <i>et al.</i> [35]	<u>37.93</u> /0.9452/ <u>0.115</u>	<u>0.2481</u> /26.874	28.33/0.8494/ 0.270	0.3391/ <u>21.762</u>
Ours	TMRNet	38.19/0.9488/0.112	<u>0.2426</u> / 27.995	28.91/0.8572/0.273	0.3687/21.808

Table 3: Comparison of inference time with the recent state-of-the-art methods when generating a 1920×1080 raw image on BracketIRE task.

Method	BIPNet [19]	Burstormer [20]	RBSR [86]	HDR-Tran. [50]	SCTNet [75]	Kim <i>et al.</i> [35]	TMRNet
Time (s)	6.166	2.357	1.467	1.897	3.894	1.672	1.425

5.2 Evaluation and Comparison Configurations

Evaluation Configurations. For quantitative evaluations and visualizations, we first convert raw results to linear RGB space through a post-processing pipeline and then tone-map them with Eq. (5), getting 16-bit RGB images. All metrics are computed on the RGB images. For synthetic experiments, we adopt PSNR, SSIM [80], and LPIPS [101] metrics. For real-world ones, we employ no-reference metrics *i.e.*, CLIP-IQA [76] and MUSIQ [34].

Comparison Configurations. We compare the proposed method with 10 related state-of-the-art networks, including 5 burst processing ones (*i.e.*, DBSR [4], MFIR [5], BIPNet [19], Burstormer [20] and RBSR [86]) and 5 HDR reconstruction ones (*i.e.*, AHDRNet [92], HDRGAN [61], HDR-Tran. [50], SCTNet [75] and Kim *et al.* [35]). For a fair comparison, we modify their models to adapt inputs with 5 frames, and retrain them on our synthetic pairs following the formulation in Sec. 3.1. When testing real-world images, their trained models are deployed directly, while our models are fine-tuned on real-world training images with the proposed self-supervised adaptation method.

5.3 Experimental Results

Results on Synthetic Dataset. We summarize the quantitative results in Tab. 2. On BracketIRE task, we achieve 0.31dB and 0.26dB PSNR gains than RBSR [86] and Kim *et al.* [35], respectively, which are the latest state-of-the-art methods. On BracketIRE+ task, the improvements are 0.21dB and 0.58dB,

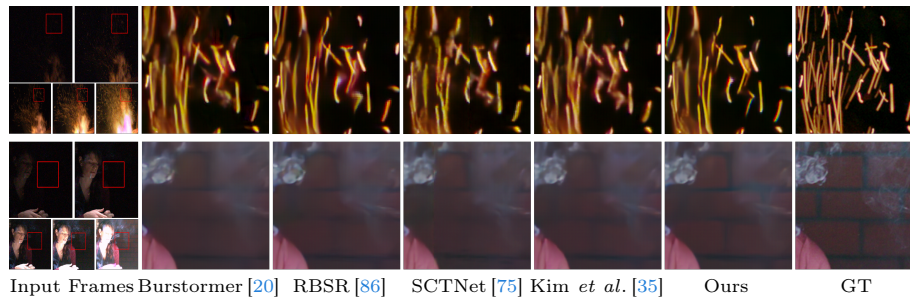


Fig. 4: Visual comparison on the synthetic dataset of BracketIRE task. Our method restores sharper edges and clearer details.

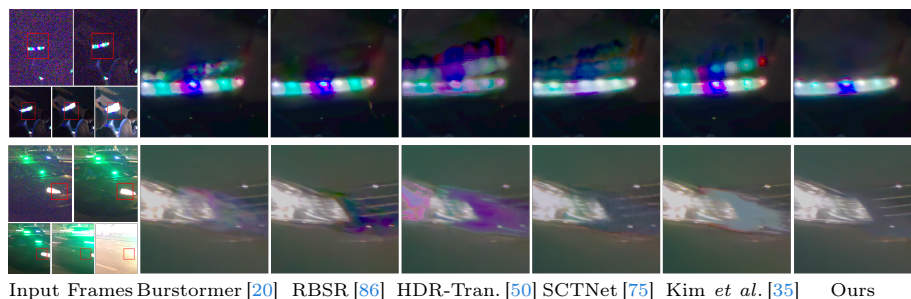


Fig. 5: Visual comparison on the real-world dataset of BracketIRE task. Our results have fewer ghosting artifacts.

respectively. It demonstrates the effectiveness of our TMRNet, which handles the varying degradations of multi-exposure images by deploying frame-specific parameters. Moreover, the qualitative results in Fig. 4 show that TMRNet recovers more realistic details than others.

Results on Real-World Dataset. We outperform the second-place competitor by a large margin on MUSIQ on BracketIRE task, and we also achieve the highest no-reference scores on BracketIRE+ task. But note that the no-reference metrics are not completely stable and are only used for auxiliary evaluation. The actual visual results can better demonstrate the effect of different methods. As shown in Fig. 5, applying other models trained on synthetic data to the real world easily produces undesirable artifacts. Benefiting from the proposed self-supervised real-image adaptation, our results have fewer artifacts and more satisfactory content. Visual comparisons on BracketIRE+ task can be seen in the suppl.

Inference Time. We provide comparisons of the inference time in Tab. 3. It can be seen that our method has a similar time with RBSR [86], and a shorter time than recent state-of-the-art ones, *i.e.*, BIPNet [19], Burstormer [20], HDR-Tran. [50], SCTNet [75] and Kim *et al.* [35]. Overall, our method maintains good efficiency while improving performance compared to recent state-of-the-art methods. More comparisons can be seen in the suppl.

Table 4: Comparison with burst processing manner. $\{\mathbf{Y}_i^b\}_{b=1}^5$ denote the 5 burst images with exposure time Δt_i .

Input	BracketIRE	BracketIRE+
	PSNR \uparrow /SSIM \uparrow /LPIPS \downarrow	PSNR \uparrow /SSIM \uparrow /LPIPS \downarrow
$\{\mathbf{Y}_1^b\}_{b=1}^5$	31.34/0.8516/0.273	26.06/0.7515/0.421
$\{\mathbf{Y}_2^b\}_{b=1}^5$	<u>34.61/0.9184/0.170</u>	<u>27.80/0.8134/0.350</u>
$\{\mathbf{Y}_3^b\}_{b=1}^5$	<u>31.77/0.9267/0.141</u>	<u>27.34/0.8428/0.304</u>
$\{\mathbf{Y}_4^b\}_{b=1}^5$	26.14/0.8854/0.210	24.10/0.8087/0.383
$\{\mathbf{Y}_5^b\}_{b=1}^5$	20.04/0.8255/0.354	20.77/0.7922/0.442
$\{\mathbf{Y}_i\}_{i=1}^5$	38.19/0.9488/0.112	28.91/0.8572/0.273

Table 5: Effect of number of input multi-exposure frames.

Input	BracketIRE	BracketIRE+
	PSNR \uparrow /SSIM \uparrow /LPIPS \downarrow	PSNR \uparrow /SSIM \uparrow /LPIPS \downarrow
\mathbf{Y}_1	28.76/0.8094/0.348	24.48/0.7138/0.472
$\{\mathbf{Y}_i\}_{i=1}^2$	32.75/0.8815/0.240	26.94/0.7847/0.394
$\{\mathbf{Y}_i\}_{i=1}^3$	35.68/0.9223/0.166	28.42/0.8291/0.328
$\{\mathbf{Y}_i\}_{i=1}^4$	<u>37.04/0.9420/0.129</u>	<u>28.77/0.8485/0.289</u>
$\{\mathbf{Y}_i\}_{i=1}^5$	38.19/0.9488/0.112	28.91/0.8572/0.273

6 Ablation Study

6.1 Comparison with Burst Imaging

To validate the effectiveness of leveraging multi-exposure frames, we compare our method with burst imaging manner that employs multiple images with the same exposure. For each exposure time Δt_i , we use our data simulation pipeline to construct 5 burst images $\{\mathbf{Y}_i^b\}_{b=1}^5$ as inputs. The quantitative results are shown in Tab. 4. It can be seen that the models using moderate exposure bursts (*e.g.*, \mathbf{Y}_2 and \mathbf{Y}_3) achieve better results, as these bursts take good trade-offs between noise and blur, as well as overexposure and underexposure. Nevertheless, their results are still weaker than ours by a wide margin, mainly due to the limited dynamic range of the input bursts.

6.2 Effect of Number of Input Frames

To validate the effect of the number of input frames, we conduct experiments by removing relatively higher exposure frames one by one, as shown in Tab. 5. Naturally, more frames result in better performance. It is worth noting that using $\{\mathbf{Y}_i\}_{i=1}^4$ is already better than all burst manners in Tab. 4, which further indicates the advantages of combining multi-exposure images. In addition, adding images with longer exposure will lead to exponential increases of shooting time. And the higher the exposure time, the less valuable content in the image. Considering these two aspects, we only adopt 5 frames. Furthermore, we conduct experiments with more combinations of multi-exposure images in the suppl.

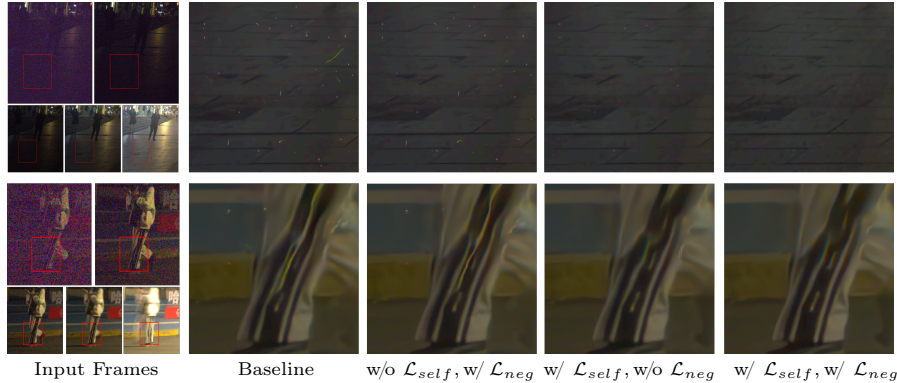


Fig. 6: Effect of loss terms for self-supervised real-image adaptation. Our results have fewer speckling and ghosting artifacts. Please zoom in for better observation.

Table 6: Effect of a_c and a_s , which denotes the number of common and specific blocks, respectively. We maintain the sum of a_c and a_s unchanged, *i.e.*, these models have similar inference costs.

α_c	α_s	BracketIRE			BracketIRE+		
		PSNR \uparrow /SSIM \uparrow /LPIPS \downarrow			PSNR \uparrow /SSIM \uparrow /LPIPS \downarrow		
0	40	37.80/0.9449/0.123			28.68/0.8541/0.279		
8	32	37.86/ <u>0.9473</u> /0.117			28.90/0.8562/ <u>0.274</u>		
16	24	38.19/0.9488/0.112			<u>28.91</u> / 0.8572 / 0.273		
24	16	<u>38.10</u> /0.9468/ <u>0.115</u>			28.93 /0.8555/0.275		
32	8	37.85/0.9467/0.118			28.87/ <u>0.8566</u> /0.279		
40	0	37.88/0.9453/0.119			28.70/0.8549/0.279		

6.3 Effect of TMRNet

We change the depths of common and specific modules to explore the effect of temporal modulation in TMRNet. For a fair comparison, we keep the total depth the same. From Tab. 6, completely taking common module or specific one does not achieve satisfactory results, as the former ignores the degradation difference of multi-exposure images while the latter may be difficult to optimize. Allocating appropriate depths to both modules can perform better. In addition, we also conduct experiments by changing the depths of the two modules independently in the suppl.

6.4 Effect of Self-Supervised Adaptation

To validate the effectiveness of the proposed adaptation method, we regard TMRNet trained on synthetic pairs as a baseline, and conduct experiments by removing \mathcal{L}_{self} and \mathcal{L}_{neg} respectively in Eq. (12). From the visual comparison in Fig. 6, \mathcal{L}_{self} plays the main role in alleviating artifacts, while using \mathcal{L}_{neg} alone has a limited effect. Nevertheless, combining \mathcal{L}_{self} and \mathcal{L}_{neg} contributes to achieving better results with fewer artifacts. In addition, without \mathcal{L}_{ema} , the self-supervised fine-tuning would lead to a trivial solution, thus collapsing.

7 Conclusion

Existing multi-image processing methods typically focus exclusively on either restoration or enhancement, which are insufficient for obtaining visually appealing images with clear content in low-light conditions. Motivated by the complementary potential of multi-exposure images in denoising, deblurring, HDR reconstruction, and SR, we proposed to utilize exposure bracketing photography to unify these image restoration and enhancement tasks. Specifically, we suggested a solution that initially pre-trains the model with synthetic pairs and subsequently adapts it to unlabeled real-world images, where a temporally modulated recurrent network and a self-supervised adaptation method are presented. Moreover, we constructed a data simulation pipeline for synthesizing pairs and collected real-world images from 200 nighttime scenarios. Experiments on both datasets show our method achieves better results than state-of-the-arts.

Supplementary Material

The content of the supplementary material involves:

- Details of synthetic noise in Appendix A.
- Quantitative comparisons on cropped images on synthetic dataset in Appendix B.
- Comparison of computational costs in Appendix C.
- Effect of multi-exposure combinations in Appendix D.
- Effect of TMRNet in Appendix E.
- Effect of self-supervised adaptation in Appendix F.
- More visual comparisons in Appendix G.
- Applications and limitations in Appendix H.

A Details of Synthetic Noise

The noise in raw images is mainly composed of shot and read noise [7]. Shot noise can be modeled as a Poisson random variable whose mean is the true light intensity measured in photoelectrons. Read noise can be approximated as a Gaussian random variable with a zero mean and a fixed variance. The combination of shot and read noise can be approximated as a single heteroscedastic Gaussian random variable \mathbf{N} , which can be written as,

$$\mathbf{N} \sim \mathcal{N}(\mathbf{0}, \lambda_{read} + \lambda_{shot}\mathbf{X}), \quad (\text{A})$$

where \mathbf{X} is the clean signal value. λ_{read} and λ_{shot} are determined by sensor’s analog and digital gains.

In order to make our synthetic noise as close as possible to the collected real-world image noise, we adopt noise parameters of the main camera sensor in Xiaomi 10S smartphone, and they (*i.e.*, λ_{shot} and λ_{read}) can be found in the metadata of raw image file. Specifically, the ISO of all captured real-world images is set to 1,600. At this ISO, $\lambda_{shot} \approx 2.42 \times 10^{-3}$ and $\lambda_{read} \approx 1.79 \times 10^{-5}$. Moreover, in order to synthesize noise with various levels, we uniformly sample the parameters from ISO = 800 to ISO = 3,200. Finally, λ_{read} and λ_{shot} can be expressed as,

$$\begin{aligned} \log(\lambda_{shot}) &\sim \mathcal{U}(\log(0.0012), \log(0.0048)), \\ \log(\lambda_{read}) \mid \log(\lambda_{shot}) &\sim \mathcal{N}(1.869 \log(\lambda_{shot}) + 0.3276, 0.3), \end{aligned} \quad (\text{B})$$

where $\mathcal{U}(a, b)$ represents a uniform distribution within the interval $[a, b]$.

Table A: Quantitative comparison on full images and cropped images in synthetic dataset. The metrics of cropped images are calculated on the results that exclude the surrounding 10 invalid pixels and 16 invalid pixels on BracketIRE and BracketIRE+ tasks, respectively. The top two results are marked in **bold** and underlined, respectively.

Method	BracketIRE		BracketIRE+		
	Full Images	Cropped Images	Full Images	Cropped Images	
	PSNR \uparrow /SSIM \uparrow /LPIPS \downarrow	PSNR \uparrow /SSIM \uparrow /LPIPS \downarrow	PSNR \uparrow /SSIM \uparrow /LPIPS \downarrow	PSNR \uparrow /SSIM \uparrow /LPIPS \downarrow	
Burst Processing	DBSR [4]	34.03/0.9012/0.188	35.13/0.9092/0.188	28.21/0.8364/0.338	29.79/0.8546/0.335
	MFIR [5]	34.67/0.9121/0.175	35.64/0.9161/0.177	28.40/0.8424/0.320	30.06/0.8591/0.319
Networks	BIPNet [19]	35.98/0.9314/0.145	36.92/0.9331/0.148	28.41/0.8432/0.326	30.02/0.8582/0.324
	Burstormer [20]	36.62/0.9378/0.140	37.06/0.9344/0.151	28.37/0.8460/0.301	29.99/0.8617/0.300
	RBSR [86]	37.88/ <u>0.9453</u> /0.119	<u>38.82</u> /0.9464/0.121	<u>28.70</u> / <u>0.8549</u> /0.279	<u>30.49</u> / <u>0.8713</u> /0.275
HDR Reconstruction	AHDRNet [92]	36.32/0.9273/0.154	36.68/0.9279/0.158	28.17/0.8422/0.309	29.86/0.8589/0.308
	HDRGAN [61]	35.05/0.9161/0.175	35.94/0.9177/0.181	28.35/0.8423/0.338	30.00/0.8590/0.337
Networks	HDR-Tran. [50]	36.54/0.9341/0.127	37.62/0.9356/0.129	28.15/0.8482/0.281	30.18/0.8662/0.279
	SCTNet [75]	36.90/0.9437/0.120	37.47/0.9443/0.122	28.28/0.8461/0.282	30.13/0.8644/0.281
	Kim <i>et al.</i> [35]	<u>37.93</u> / <u>0.9452</u> / <u>0.115</u>	<u>38.73</u> / <u>0.9465</u> / <u>0.117</u>	28.33/0.8494/ 0.270	30.28/0.8658/ 0.268
Ours	TMRNet	38.19 / 0.9488 / 0.112	39.06 / 0.9498 / 0.115	28.91 / 0.8572 / <u>0.273</u>	30.65 / 0.8725 / <u>0.270</u>

B Quantitative Comparisons on Cropped Images on Synthetic Dataset

The images in the synthetic dataset have a black border with a determined number of pixels. During training, we avoid feeding the network with patches containing the black border. However, in the main paper, evaluation is performed on full images containing the black border. It is a little inappropriate, as the black border does not contain valid pixels and the border pixels affect the inference results. Here, we additionally evaluate the metrics of the cropped image. For BracketIRE and BracketIRE+ tasks, 10 and 4 pixels around the original input image are excluded, while 10 and 16 pixels around the corresponding ground-truth image are excluded, respectively. The results are as shown in Tab. A. It can be seen that the overall trend is similar to the test results on the full images, and our TMRNet still maintains a certain advantage compared to other methods.

C Comparison of Computational Costs

We provide comparisons of the inference time, as well as the number of FLOPs and model parameters in Tab. B. We mainly focus on inference time, which can directly reflect the method’s efficiency for practical applicability. It can be seen that our method has a similar time with RBSR [86], and a shorter time than recent state-of-the-art ones, *i.e.*, BIPNet [19], Burstormer [20], HDR-Tran. [50], SCTNet [75] and Kim *et al.* [35]. Overall, our method maintains good efficiency while improving performance compared to recent state-of-the-art methods.

D Effect of Multi-Exposure Combinations

We conduct experiments with different combinations of multi-exposure images in the Tab. C. Naturally, the more frames, the better the results. Simultaneously,

Table B: Comparison of #parameters and computational costs with state-of-the-art methods when generating a 1920×1080 raw image on BracketIRE task. Note that the inference time can better illustrate the method’s efficiency than #parameters and #FLOPs for practical applicability.

Method	#Params (M)	#FLOPs (G)	Time (ms)
DBSR [4]	12.90	16,120	850
MFIR [5]	12.03	18,927	974
BIPNet [19]	6.28	135,641	6,166
Burstormer [20]	3.11	9,200	2,357
RBSR [86]	5.64	19,440	1,467
AHDRNet [92]	2.04	2,053	208
HDRGAN [61]	9.77	2,410	158
HDR-Tran. [50]	1.69	1,710	1,897
SCTNet [75]	5.02	5,145	3,894
Kim <i>et al.</i> [35]	22.74	5,068	1,672
TMRNet	13.29	20,040	1,425

Table C: Effect of multi-exposure image combinations on BracketIRE task.

Input	PSNR \uparrow / SSIM \uparrow / LPIPS \downarrow
$\{\mathbf{Y}_1, \mathbf{Y}_2, \mathbf{Y}_3\}$	35.68 / 0.9223 / 0.166
$\{\mathbf{Y}_1, \mathbf{Y}_3, \mathbf{Y}_5\}$	35.40 / 0.9204 / 0.173
$\{\mathbf{Y}_2, \mathbf{Y}_3, \mathbf{Y}_4\}$	34.60 / 0.9230 / 0.169
$\{\mathbf{Y}_3, \mathbf{Y}_4, \mathbf{Y}_5\}$	31.00 / 0.9166 / 0.174
$\{\mathbf{Y}_1, \mathbf{Y}_2, \mathbf{Y}_3, \mathbf{Y}_4\}$	37.04 / 0.9420 / 0.129
$\{\mathbf{Y}_2, \mathbf{Y}_3, \mathbf{Y}_4, \mathbf{Y}_5\}$	35.43 / 0.9388 / 0.134
$\{\mathbf{Y}_1, \mathbf{Y}_2, \mathbf{Y}_3, \mathbf{Y}_4, \mathbf{Y}_5\}$	38.19 / 0.9488 / 0.112

it can be seen that long-exposure images are more difficult to process than short-exposure images, as the longer the exposure time, the more severe the blur.

In this work, we adopt the frame number $T = 5$ and exposure time ratio $S = 4$, as it can cover most of the dynamic range using fewer frames. Additionally, without considering shooting and computational costs, it is foreseeable that a larger T or smaller S would perform better when keeping the overall dynamic range the same.

E Effect of TMRNet

For TMRNet, we conduct experiments by changing the depths of the common and specific blocks independently, whose results are shown in Tab. D and Tab. E, respectively. Denote the number of common and specific blocks by a_c and a_s , respectively. On the basis of $a_c = 16$ and $a_s = 24$, adding their depths did not

Table D: Effect of depth of specific blocks while keeping common blocks the same on BracketIRE task. a_c and a_s denote the number of common and specific blocks, respectively.

α_c	α_s	Time (ms)	PSNR \uparrow / SSIM \uparrow / LPIPS \downarrow
16	0	808	37.50 / 0.9436 / 0.125
16	8	1,016	37.65 / 0.9452 / 0.121
16	16	1,224	<u>38.09</u> / 0.9463 / 0.116
16	24	1,425	38.19 / 0.9488 / 0.112
16	32	1,633	38.02 / <u>0.9479</u> / <u>0.113</u>

Table E: Effect of depth of common blocks while keeping specific blocks the same on BracketIRE task. a_c and a_s denote the number of common and specific blocks, respectively.

α_c	α_s	Time (ms)	PSNR \uparrow / SSIM \uparrow / LPIPS \downarrow
0	24	1,015	37.71 / 0.9450 / 0.123
8	24	1,219	37.68 / 0.9457 / 0.121
16	24	1,425	38.19 / 0.9488 / 0.112
24	24	1,637	<u>37.96</u> / <u>0.9477</u> / <u>0.117</u>

bring significant improvement while increasing the inference time. We speculate that it could be attributed to the difficulty of optimization for deeper recurrent networks.

F Effect of Self-Supervised Adaptation

In the main text, to validate the effectiveness of the proposed adaptation method, we regard TMRNet trained on synthetic pairs as a baseline, and conduct experiments by removing \mathcal{L}_{self} and \mathcal{L}_{neg} respectively. Here we provide the quantitative comparisons in Tab. F. It can be seen that combining \mathcal{L}_{self} and \mathcal{L}_{neg} can bring both CLIP-IQA [76] and MUSIQ [34] improvements. In addition, we empirically adjust their weights and conduct experiments with different λ_{self} and λ_{neg} . From Tabs. G and H, the effect of their weights on the results is acceptable.

Nevertheless, the no-reference metrics are not completely stable and are only used for auxiliary evaluation. Visual quality can better reflect the effect of different loss terms. We provide more visual comparisons in Fig. A. It can be seen that both \mathcal{L}_{self} and \mathcal{L}_{neg} can play a role in the adaptation.

G More Visual Comparisons

We first provide more visual comparisons on BracketIRE+ task. Figs. B and C show the qualitative comparisons on the synthetic images. Figs. D and E show

Table F: Effect of loss terms for self-supervised real-image adaptation. ‘-’ denotes the baseline model trained on synthetic pairs. ‘NaN’ implies the training collapse. The no-reference metrics are not completely stable and are provided only for auxiliary evaluation.

\mathcal{L}_{ema}	\mathcal{L}_{self}	\mathcal{L}_{neg}	CLIP-IQA \uparrow / MUSIQ \uparrow
-	-	-	0.2083 / 27.257
\times	\checkmark	\checkmark	NaN / NaN
\checkmark	\checkmark	\times	0.2435 / 26.809
\checkmark	\times	\checkmark	0.2172 / 28.157
\checkmark	\checkmark	\checkmark	<u>0.2426</u> / <u>27.995</u>

Table G: Effect of λ_{self} .

λ_{self}	CLIP-IQA \uparrow / MUSIQ \uparrow
0.5	0.2279 / <u>27.899</u>
2	0.2445 / 27.522
1	<u>0.2426</u> / 27.995

Table H: Effect of λ_{neg} .

λ_{neg}	CLIP-IQA \uparrow / MUSIQ \uparrow
0.1	<u>0.2419</u> / 27.352
0.3	0.2255 / 28.051
0.2	0.2426 / <u>27.995</u>

the qualitative comparisons on the real-world images. It can be seen that our method generates more photo-realistic images with fewer artifacts than others.

Moreover, in order to observe the effect of dynamic range enhancement, we provide some full-image results from real-world dataset. Note that the size of the original full images is very large, and here we downsample them for display. Fig. F shows the full-image visualization results on BracketIRE task. Fig. G shows the full-image visualization results on BracketIRE+ task. Our results preserve both bright and dark details, showing a higher dynamic range.

H Applications and Limitations

Applications. A significant application of this work is HDR imaging at night, especially in dynamic environments, aiming to obtain noise-free, blur-free, and HDR images. Such images can clearly show both bright and dark details in nighttime scenes. The application is not only challenging but also practically valuable. We also experiment with it on a smartphone (*i.e.*, Xiaomi 10S), as shown in Figs. F and G.

Limitations. Given the diverse imaging characteristics (especially noise model parameters) of various sensors, our method necessitates tailored training for each sensor. In other words, our model trained on images from one sensor may exhibit limited generalization ability when applied to other sensors. We leave the investigation of a more general model to future work.

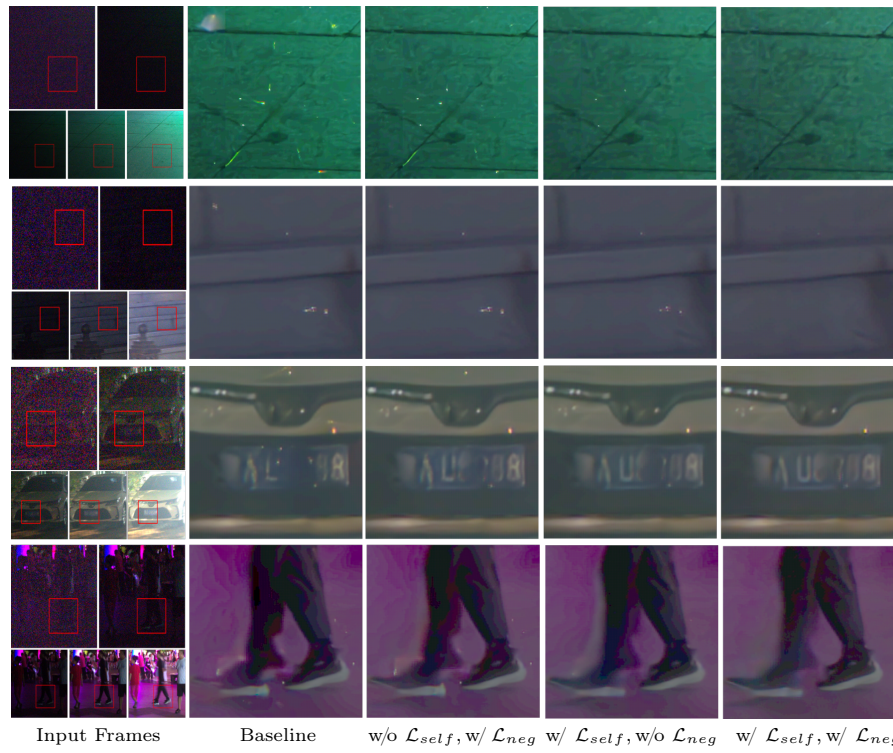


Fig. A: Effect of loss terms for self-supervised real-image adaptation. Our results have fewer speckling and ghosting artifacts. Please zoom in for better observation.

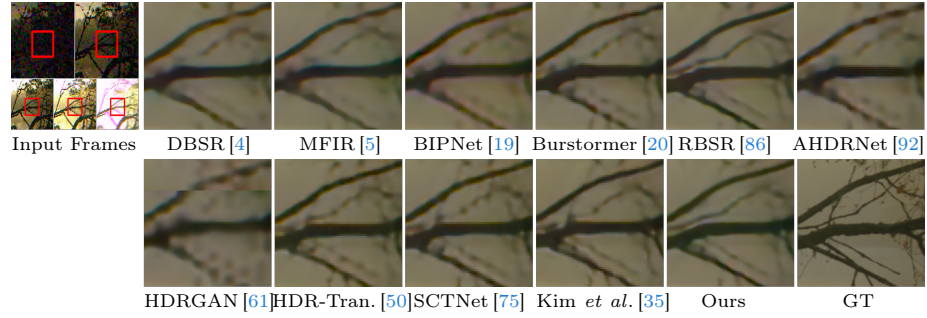


Fig. B: Visual comparison on the synthetic dataset of BracketIRE+ task. Our result restores clearer details. Please zoom in for better observation.

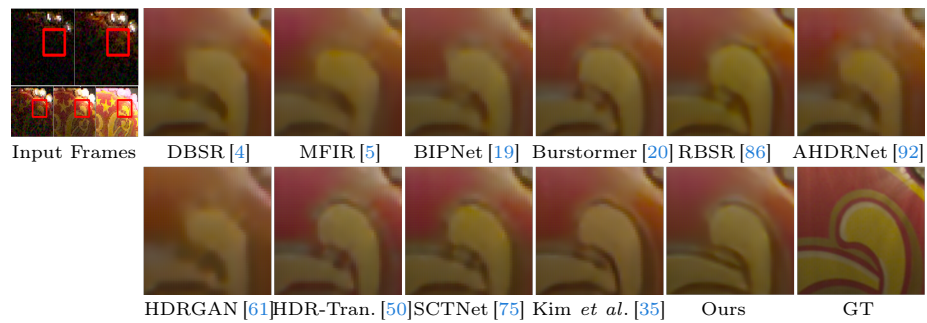


Fig. C: Visual comparison on the synthetic dataset of BracketIRE+ task. Our result restores more fidelity content. Please zoom in for better observation.

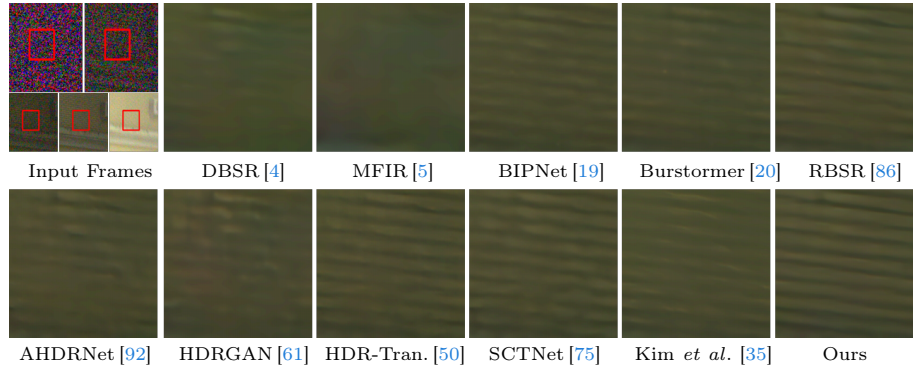


Fig. D: Visual comparison on the real-world dataset of BracketIRE+ task. Our result restores clearer textures. Please zoom in for better observation.

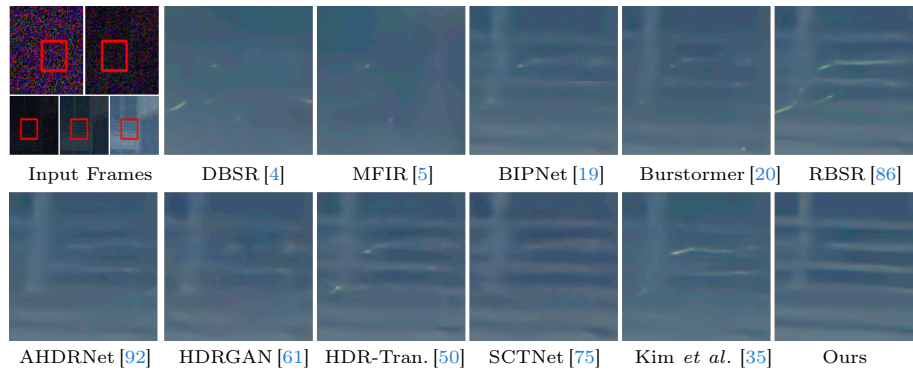


Fig. E: Visual comparison on the real-world dataset of BracketIRE+ task. Our result has fewer artifacts. Please zoom in for better observation.



Fig. F: Full-image results on the real-world dataset of BracketIRE task. Our results preserve both the bright areas in short-exposure images and the dark areas in long-exposure images. Note that the size of the original full images is very large, and here we downsample them for display. Please zoom in for better observation.

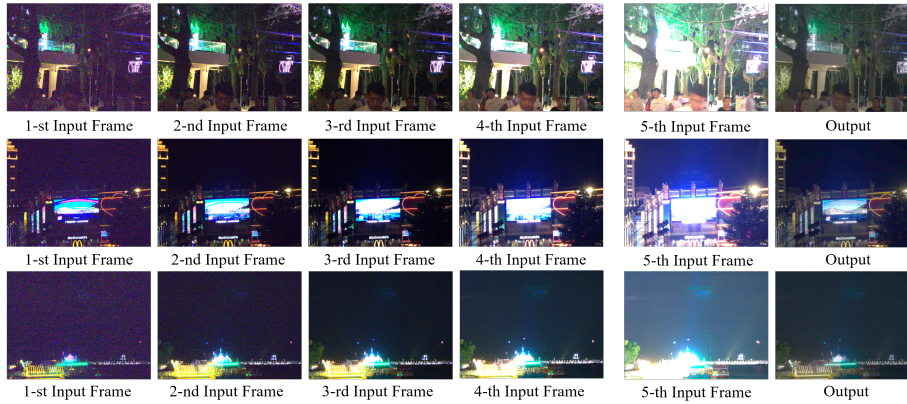


Fig. G: Full-image results on the real-world dataset of BracketIRE+ task. Our results preserve both the bright areas in short-exposure images and the dark areas in long-exposure images. Note that the size of the original full images is very large, and here we downsample them for display. Please zoom in for better observation.

References

1. Abdelhamed, A., Affi, M., Timofte, R., Brown, M.S.: Ntire 2020 challenge on real image denoising: Dataset, methods and results. In: CVPR Workshops (2020)
2. Aittala, M., Durand, F.: Burst image deblurring using permutation invariant convolutional neural networks. In: ECCV (2018)
3. Bhat, G., Danelljan, M., Timofte, R., Cao, Y., Cao, Y., Chen, M., Chen, X., Cheng, S., Dudhane, A., Fan, H., et al.: Ntire 2022 burst super-resolution challenge. In: CVPR Workshops (2022)
4. Bhat, G., Danelljan, M., Van Gool, L., Timofte, R.: Deep burst super-resolution. In: CVPR (2021)
5. Bhat, G., Danelljan, M., Yu, F., Van Gool, L., Timofte, R.: Deep reparametrization of multi-frame super-resolution and denoising. In: CVPR (2021)
6. Bhat, G., Gharbi, M., Chen, J., Van Gool, L., Xia, Z.: Self-supervised burst super-resolution. In: ICCV (2023)
7. Brooks, T., Mildenhall, B., Xue, T., Chen, J., Sharlet, D., Barron, J.T.: Unprocessing images for learned raw denoising. In: CVPR (2019)
8. Chan, K.C., Wang, X., Yu, K., Dong, C., Loy, C.C.: Basicvsr: The search for essential components in video super-resolution and beyond. In: CVPR (2021)
9. Chan, K.C., Zhou, S., Xu, X., Loy, C.C.: Basicvsr++: Improving video super-resolution with enhanced propagation and alignment. In: CVPR (2022)
10. Chang, M., Feng, H., Xu, Z., Li, Q.: Low-light image restoration with short-and long-exposure raw pairs. IEEE TMM (2021)
11. Chen, S.K., Yen, H.L., Liu, Y.L., Chen, M.H., Hu, H.N., Peng, W.H., Lin, Y.Y.: Learning continuous exposure value representations for single-image hdr reconstruction. In: ICCV (2023)
12. Chi, Y., Zhang, X., Chan, S.H.: Hdr imaging with spatially varying signal-to-noise ratios. In: CVPR (2023)
13. Cho, S.J., Ji, S.W., Hong, J.P., Jung, S.W., Ko, S.J.: Rethinking coarse-to-fine approach in single image deblurring. In: ICCV (2021)
14. Dai, J., Qi, H., Xiong, Y., Li, Y., Zhang, G., Hu, H., Wei, Y.: Deformable convolutional networks. In: ICCV (2017)
15. Delbracio, M., Sapiro, G.: Burst deblurring: Removing camera shake through fourier burst accumulation. In: CVPR (2015)
16. Deudon, M., Kalaitzis, A., Goytom, I., Arefin, M.R., Lin, Z., Sankaran, K., Michalski, V., Kahou, S.E., Cornebise, J., Bengio, Y.: Highres-net: Recursive fusion for multi-frame super-resolution of satellite imagery. arXiv preprint arXiv:2002.06460 (2020)
17. Dewil, V., Anger, J., Davy, A., Ehret, T., Facciolo, G., Arias, P.: Self-supervised training for blind multi-frame video denoising. In: WACV (2021)
18. Dong, C., Loy, C.C., He, K., Tang, X.: Image super-resolution using deep convolutional networks. TPAMI (2015)
19. Dudhane, A., Zamir, S.W., Khan, S., Khan, F.S., Yang, M.H.: Burst image restoration and enhancement. In: CVPR (2022)
20. Dudhane, A., Zamir, S.W., Khan, S., Khan, F.S., Yang, M.H.: Burstormer: Burst image restoration and enhancement transformer. CVPR (2023)
21. Ehret, T., Davy, A., Morel, J.M., Facciolo, G., Arias, P.: Model-blind video denoising via frame-to-frame training. In: CVPR (2019)
22. Eilertsen, G., Kronander, J., Denes, G., Mantiuk, R.K., Unger, J.: Hdr image reconstruction from a single exposure using deep cnns. ACM TOG (2017)

23. Ernst, M., Wronski, B.: Hdr+ with bracketing on pixel phones (2021), <https://blog.research.google/2021/04/hdr-with-bracketing-on-pixel-phones.html>
24. Froehlich, J., Grandinetti, S., Eberhardt, B., Walter, S., Schilling, A., Brendel, H.: Creating cinematic wide gamut hdr-video for the evaluation of tone mapping operators and hdr-displays. In: Digital photography X (2014)
25. Games, R.U.: Proshot (2023), <https://www.riseupgames.com/proshot>
26. Godard, C., Matzen, K., Uyttendaele, M.: Deep burst denoising. In: ECCV (2018)
27. Guo, S., Yan, Z., Zhang, K., Zuo, W., Zhang, L.: Toward convolutional blind denoising of real photographs. In: CVPR (2019)
28. Guo, S., Yang, X., Ma, J., Ren, G., Zhang, L.: A differentiable two-stage alignment scheme for burst image reconstruction with large shift. In: CVPR (2022)
29. Hasinoff, S.W., Durand, F., Freeman, W.T.: Noise-optimal capture for high dynamic range photography. In: CVPR (2010)
30. Hasinoff, S.W., Sharlet, D., Geiss, R., Adams, A., Barron, J.T., Kainz, F., Chen, J., Levoy, M.: Burst photography for high dynamic range and low-light imaging on mobile cameras. ACM TOG (2016)
31. He, K., Zhang, X., Ren, S., Sun, J.: Deep residual learning for image recognition. In: CVPR (2016)
32. Huang, Z., Zhang, T., Heng, W., Shi, B., Zhou, S.: Real-time intermediate flow estimation for video frame interpolation. In: ECCV (2022)
33. Kalantari, N.K., Ramamoorthi, R., et al.: Deep high dynamic range imaging of dynamic scenes. ACM TOG (2017)
34. Ke, J., Wang, Q., Wang, Y., Milanfar, P., Yang, F.: Musiq: Multi-scale image quality transformer. In: ICCV (2021)
35. Kim, J., Kim, M.H.: Joint demosaicing and deghosting of time-varying exposures for single-shot hdr imaging. In: ICCV (2023)
36. Krull, A., Buchholz, T.O., Jug, F.: Noise2void-learning denoising from single noisy images. In: CVPR (2019)
37. Lai, W.S., Shih, Y., Chu, L.C., Wu, X., Tsai, S.F., Krainin, M., Sun, D., Liang, C.K.: Face deblurring using dual camera fusion on mobile phones. ACM TOG (2022)
38. Laine, S., Karras, T., Lehtinen, J., Aila, T.: High-quality self-supervised deep image denoising. NeurIPS (2019)
39. Lecouat, B., Eboli, T., Ponce, J., Mairal, J.: High dynamic range and super-resolution from raw image bursts. ACM TOG (2022)
40. Lecouat, B., Ponce, J., Mairal, J.: Lucas-kanade reloaded: End-to-end super-resolution from raw image bursts. In: ICCV (2021)
41. Ledig, C., Theis, L., Huszár, F., Caballero, J., Cunningham, A., Acosta, A., Aitken, A., et al.: Photo-realistic single image super-resolution using a generative adversarial network. In: CVPR (2017)
42. Lee, S., An, G.H., Kang, S.J.: Deep recursive hdri: Inverse tone mapping using generative adversarial networks. In: ECCV (2018)
43. Lehtinen, J., Munkberg, J., Hasselgren, J., Laine, S., Karras, T., Aittala, M., Aila, T.: Noise2noise: Learning image restoration without clean data. In: ICML (2018)
44. Li, Y., Zhang, Y., Timofte, R., Van Gool, L., Tu, Z., Du, K., Wang, H., Chen, H., Li, W., Wang, X., et al.: Ntire 2023 challenge on image denoising: Methods and results. In: CVPR Workshops (2023)
45. Liang, J., Cao, J., Sun, G., Zhang, K., Van Gool, L., Timofte, R.: Swinir: Image restoration using swin transformer. In: ICCV (2021)

46. Lim, B., Son, S., Kim, H., Nah, S., Mu Lee, K.: Enhanced deep residual networks for single image super-resolution. In: CVPR Workshops (2017)
47. Liu, M., Zhang, Z., Hou, L., Zuo, W., Zhang, L.: Deep adaptive inference networks for single image super-resolution. In: ECCV Workshops (2020)
48. Liu, S., Zhang, X., Sun, L., Liang, Z., Zeng, H., Zhang, L.: Joint hdr denoising and fusion: A real-world mobile hdr image dataset. In: CVPR (2023)
49. Liu, Y.L., Lai, W.S., Chen, Y.S., Kao, Y.L., Yang, M.H., Chuang, Y.Y., Huang, J.B.: Single-image hdr reconstruction by learning to reverse the camera pipeline. In: CVPR (2020)
50. Liu, Z., Wang, Y., Zeng, B., Liu, S.: Ghost-free high dynamic range imaging with context-aware transformer. In: ECCV (2022)
51. Loshchilov, I., Hutter, F.: Sgdr: Stochastic gradient descent with warm restarts. arXiv:1608.03983 (2016)
52. Loshchilov, I., Hutter, F.: Decoupled weight decay regularization. arXiv:1711.05101 (2017)
53. Luo, Z., Li, Y., Cheng, S., Yu, L., Wu, Q., Wen, Z., Fan, H., Sun, J., Liu, S.: Bsrt: Improving burst super-resolution with swin transformer and flow-guided deformable alignment. In: CVPR (2022)
54. Mao, X., Liu, Y., Liu, F., Li, Q., Shen, W., Wang, Y.: Intriguing findings of frequency selection for image deblurring. In: AAAI (2023)
55. Mehta, N., Dudhane, A., Murala, S., Zamir, S.W., Khan: Gated multi-resolution transfer network for burst restoration and enhancement. CVPR (2023)
56. Mildenhall, B., Barron, J.T., Chen, J., Sharlet, D., Ng, R., Carroll, R.: Burst denoising with kernel prediction networks. In: CVPR (2018)
57. Mustaniemi, J., Kannala, J., Matas, J., Särkkä, S., Heikkilä, J.: Lsd₂-joint denoising and deblurring of short and long exposure images with cnns. In: BMVC (2020)
58. Nah, S., Baik, S., Hong, S., Moon, G., Son, S., Timofte, R., Mu Lee, K.: Ntire 2019 challenge on video deblurring and super-resolution: Dataset and study. In: CVPR Workshops (2019)
59. Nah, S., Kim, T.H., Lee, K.M.: Deep multi-scale convolutional neural network for dynamic scene deblurring. In: CVPR (2017)
60. Nazarczuk, M., Catley-Chandar, S., Leonardis, A., Pellitero, E.P.: Self-supervised hdr imaging from motion and exposure cues. arXiv preprint arXiv:2203.12311 (2022)
61. Niu, Y., Wu, J., Liu, W., Guo, W., Lau, R.W.: Hdr-gan: Hdr image reconstruction from multi-exposed ldr images with large motions. IEEE TIP (2021)
62. Paszke, A., Gross, S., Massa, F., Lerer, A., Bradbury, J., et al.: Pytorch: An imperative style, high-performance deep learning library. NeurIPS (2019)
63. Peña, F.A.G., Fernández, P.D.M., Ren, T.I., Leandro, J.d.J.G., Nishihara, R.M.: Burst ranking for blind multi-image deblurring. IEEE TIP (2019)
64. Pérez-Pellitero, E., Catley-Chandar, S., Leonardis, A., Timofte, R.: Ntire 2021 challenge on high dynamic range imaging: Dataset, methods and results. In: CVPR Workshops (2021)
65. Prabhakar, K.R., Arora, R., Swaminathan, A., Singh, K.P., Babu, R.V.: A fast, scalable, and reliable deghosting method for extreme exposure fusion. In: ICCP (2019)
66. Prabhakar, K.R., Senthil, G., Agrawal, S., Babu, R.V., Gorthi, R.K.S.S.: Labeled from unlabeled: Exploiting unlabeled data for few-shot deep hdr deghosting. In: CVPR (2021)

67. Ranjan, A., Black, M.J.: Optical flow estimation using a spatial pyramid network. In: CVPR (2017)
68. Rong, X., Demandolx, D., Matzen, K., Chatterjee, P., Tian, Y.: Burst denoising via temporally shifted wavelet transforms. In: ECCV (2020)
69. Shekarforoush, S., Walia, A., Brubaker, M.A., Derpanis, K.G., Levinshtein, A.: Dual-camera joint deblurring-denoising. arXiv preprint arXiv:2309.08826 (2023)
70. Sheth, D.Y., Mohan, S., Vincent, J.L., Manzorro, R., Crozier, P.A., Khapra, M.M., Simoncelli, E.P., Fernandez-Granda, C.: Unsupervised deep video denoising. In: ICCV (2021)
71. Shi, W., Caballero, J., Huszár, F., Totz, J., Aitken, A.P., Bishop, R., Rueckert, D., Wang, Z.: Real-time single image and video super-resolution using an efficient sub-pixel convolutional neural network. In: CVPR (2016)
72. Song, J.W., Park, Y.I., Kong, K., Kwak, J., Kang, S.J.: Selective transhrdr: Transformer-based selective hdr imaging using ghost region mask. In: ECCV (2022)
73. Tan, X., Chen, H., Xu, K., Jin, Y., Zhu, C.: Deep sr-hdr: Joint learning of super-resolution and high dynamic range imaging for dynamic scenes. IEEE TMM (2021)
74. Tao, X., Gao, H., Shen, X., Wang, J., Jia, J.: Scale-recurrent network for deep image deblurring. In: CVPR (2018)
75. Tel, S., Wu, Z., Zhang, Y., Heyrman, B., Demonceaux, C., Timofte, R., Ginhac, D.: Alignment-free hdr deghosting with semantics consistent transformer. In: ICCV (2023)
76. Wang, J., Chan, K.C., Loy, C.C.: Exploring clip for assessing the look and feel of images. In: AAAI (2023)
77. Wang, R., Liu, X., Zhang, Z., Wu, X., Feng, C.M., Zhang, L., Zuo, W.: Benchmark dataset and effective inter-frame alignment for real-world video super-resolution. In: CVPRW (2023)
78. Wang, T., Xie, J., Sun, W., Yan, Q., Chen, Q.: Dual-camera super-resolution with aligned attention modules. In: ICCV (2021)
79. Wang, Y., Huang, H., Xu, Q., Liu, J., Liu, Y., Wang, J.: Practical deep raw image denoising on mobile devices. In: ECCV (2020)
80. Wang, Z., Bovik, A.C., Sheikh, H.R., Simoncelli, E.P.: Image quality assessment: from error visibility to structural similarity. TIP (2004)
81. Wang, Z., Zhang, Y., Zhang, D., Fu, Y.: Recurrent self-supervised video denoising with denser receptive field. In: ACM MM (2023)
82. Wei, K., Fu, Y., Yang, J., Huang, H.: A physics-based noise formation model for extreme low-light raw denoising. In: CVPR (2020)
83. Wei, P., Sun, Y., Guo, X., Liu, C., Li, G., Chen, J., Ji, X., Lin, L.: Towards real-world burst image super-resolution: Benchmark and method. In: ICCV (2023)
84. Wieschollek, P., Schölkopf, B., Lensch, H.P., Hirsch, M.: End-to-end learning for image burst deblurring. In: ACCV (2017)
85. Wronski, B., Garcia-Dorado, I., Ernst, M., Kelly, D., Krainin, M., Liang, C.K., Levoy, M., Milanfar, P.: Handheld multi-frame super-resolution. ACM TOG (2019)
86. Wu, R., Zhang, Z., Zhang, S., Zhang, H., Zuo, W.: Rbsr: Efficient and flexible recurrent network for burst super-resolution. In: PRCV (2023)
87. Wu, S., Xu, J., Tai, Y.W., Tang, C.K.: Deep high dynamic range imaging with large foreground motions. In: ECCV (2018)
88. Wu, X., Liu, M., Cao, Y., Ren, D., Zuo, W.: Unpaired learning of deep image denoising. In: ECCV (2020)

89. Xia, Z., Perazzi, F., Gharbi, M., Sunkavalli, K., Chakrabarti, A.: Basis prediction networks for effective burst denoising with large kernels. In: CVPR (2020)
90. Xu, R., Yao, M., Xiong, Z.: Zero-shot dual-lens super-resolution. In: CVPR (2023)
91. Yan, Q., Chen, W., Zhang, S., Zhu, Y., Sun, J., Zhang, Y.: A unified hdr imaging method with pixel and patch level. In: CVPR (2023)
92. Yan, Q., Gong, D., Shi, Q., Hengel, A.v.d., Shen, C., Reid, I., Zhang, Y.: Attention-guided network for ghost-free high dynamic range imaging. In: CVPR (2019)
93. Yan, Q., Zhang, S., Chen, W., Tang, H., Zhu, Y., Sun, J., Van Gool, L., Zhang, Y.: Smae: Few-shot learning for hdr deghosting with saturation-aware masked autoencoders. In: CVPR (2023)
94. Yuan, L., Sun, J., Quan, L., Shum, H.Y.: Image deblurring with blurred/noisy image pairs. In: SIGGRAPH (2007)
95. Zamir, S.W., Arora, A., Khan, S., Hayat, M., Khan, F.S., Yang, M.H., Shao, L.: Cycleisp: Real image restoration via improved data synthesis. In: CVPR (2020)
96. Zamir, S.W., Arora, A., Khan, S., Hayat, M., Khan, F.S., Yang, M.H., Shao, L.: Multi-stage progressive image restoration. In: CVPR (2021)
97. Zhang, J., Pan, J., Ren, J., Song, Y., Bao, L., Lau, R.W., Yang, M.H.: Dynamic scene deblurring using spatially variant recurrent neural networks. In: CVPR (2018)
98. Zhang, K., Zuo, W., Chen, Y., Meng, D., Zhang, L.: Beyond a gaussian denoiser: Residual learning of deep cnn for image denoising. IEEE TIP (2017)
99. Zhang, K., Zuo, W., Zhang, L.: Ffdnet: Toward a fast and flexible solution for cnn-based image denoising. IEEE TIP (2018)
100. Zhang, K., Zuo, W., Zhang, L.: Learning a single convolutional super-resolution network for multiple degradations. In: CVPR (2018)
101. Zhang, R., Isola, P., Efros, A.A., Shechtman, E., Wang, O.: The unreasonable effectiveness of deep features as a perceptual metric. In: CVPR (2018)
102. Zhang, Y., Li, K., Li, K., Wang, L., Zhong, B., Fu, Y.: Image super-resolution using very deep residual channel attention networks. In: ECCV (2018)
103. Zhang, Z., Wang, H., Liu, S., Wang, X., Lei, L., Zuo, W.: Self-supervised high dynamic range imaging with multi-exposure images in dynamic scenes. In: ICLR (2024)
104. Zhang, Z., Wang, R., Zhang, H., Chen, Y., Zuo, W.: Self-supervised learning for real-world super-resolution from dual zoomed observations. In: ECCV (2022)
105. Zhang, Z., Xu, R., Liu, M., Yan, Z., Zuo, W.: Self-supervised image restoration with blurry and noisy pairs. NeurIPS (2022)
106. Zhao, Y., Xu, Y., Yan, Q., Yang, D., Wang, X., Po, L.M.: D2hnet: Joint denoising and deblurring with hierarchical network for robust night image restoration. In: ECCV (2022)
107. Zou, Y., Yan, C., Fu, Y.: Rawhdr: High dynamic range image reconstruction from a single raw image. In: ICCV (2023)